Simulation of confocal microscopy through scattering media with and without time gating

Marcus Magnor

Computer Graphics Laboratory, Stanford University, Stanford, California 94305

Peter Dorn and Wolfgang Rudolph

Department of Physics and Astronomy, University of New Mexico, Albuquerque, New Mexico 87131

Received October 26, 2000; revised manuscript received May 18, 2001

An efficient and fast simulation technique is presented to calculate characteristic features of confocal imaging through scattering media. The simulation can predict the time-resolved confocal response to pulsed illumination that allows optimizing of imaging contrast when time-gating techniques are applied. Modest computational effort is sufficient to obtain contrast predictions for arbitrary numerical aperture, focus depth, pinhole size, and scattering density, while the simulation accuracy is independent of scattering density and pinhole size. In the case of isotropic scattering, our results indicate that reflection-mode confocal imaging through scattering media is limited to $\mu d \approx 3.5$ optical thicknesses for continuous-wave illumination. If time-gating is applied, imaging through scattering densities of $\mu d \approx 8$ is theoretically possible. © 2001 Optical Society of America

OCIS codes: 290.7050, 170.6920, 170.3660, 320.7100, 290.4210, 170.1790.

1. INTRODUCTION

Confocal microscopy is an established imaging technique in biology and medicine. Its inherent depth-discrimination characteristics permit noninvasive examination of objects buried under scattering layers. With increasing penetration depth, however, the image contrast degrades due to light scattered outside the focal region. Time-gating techniques can efficiently reject those stray light components that exhibit total optical path lengths different from the light scattered inside the focal region. Such techniques include linear heterodyning, as in optical coherence tomography (OCT)[1] (recently reviewed by Schmitt),[2] as well as nonlinear techniques involving ultrashort pulses.[3–5]

In order to optimize the optical parameters of confocal imaging systems for microscopy through scattering layers with and without time gates, it is necessary to develop theoretical models. While the limiting cases of single scattering[6] and diffusion[7] can be analytically modeled, no closed-form expression has yet been found to describe multiple scattering in combination with imaging optics. Monte Carlo (MC)-based computer algorithms have been developed to simulate light propagation through random scattering media.[8,9] By tracing photon trajectories inside the scattering material and through the optical system, these algorithms allow the examination of the influence of multiple scattering on confocal imaging properties in scanning microscopes. Unfortunately, time-consuming simulations are necessary to obtain statistically reliable results when applying MC methods directly to confocal microscopy.[10] Only a small fraction of photons passes through the pinhole and contributes to the confocal image signal. To improve statistics and shorten simulation time the MC simulation can be biased to assign more weight to photons that reach the detector.[11] While biased MC simulation has been shown to predict confocal imaging characteristics with acceptable computational effort, its accuracy degrades if the pinhole size approaches the confocal limit. A recent attempt to use MC methods to simulate confocal microscopy with time gating[12] does not apply to true confocal microscopy.

The aim of this paper is to introduce an efficient simulation technique for confocal imaging through scattering materials based only partly on MC simulation and, for the first time to our knowledge, to model the contrast when time gates are applied. In this study we limit ourselves to isotropic scattering as it would originate from particles much smaller than the wavelength of the light used. The simulation method allows us to determine the time-resolved response of reflection-mode confocal microscopy through turbid media subject to scattering density, pinhole size, numerical aperture, focusing depth, and duration of the time gate. The simulation accuracy is independent of the pinhole diameter and scattering density and yields reliable predictions for dense scatterers and true confocal imaging. The simulation time is also shorter than for previously reported algorithms; 7×10^8 photon paths are considered in less than 1 h on a conventional personal computer (Pentium II, 300 MHz). While we concentrate on confocal microscopy in this paper, the technique can also be applied to simulate the response of multiphoton microscopy through turbid media.

0740-3224/2001/111695-06$15.00

2. SIMULATION MODEL

To examine confocal microscopy through scattering media, the response of the optical system and the propagation of light through the scatterer must be modeled correctly. The scattering medium itself is considered as a slab of infinite thickness with isotropic scattering properties, where the anisotropy parameter $g = 0$.

Our simulation is based on the schematic diagram depicted in Fig. 1. The optical system is treated in the approximation of geometrical optics, which has been shown to realistically describe depth-discrimination properties and contrast behavior of confocal microscopy.[10,11] Stray light is optimally rejected only if the microscope is operated in the true confocal mode. Expressed in optical units,

$$u = \frac{8\pi z}{\lambda}\sin^2\frac{\alpha}{2}, \tag{1}$$

$$v = \frac{2\pi r}{\lambda}\sin\alpha, \tag{2}$$

confocal microscopy attains maximal depth resolution if the pinhole diameter v_{PH} is smaller than ≈ 2.5 optical units.[13] Here $\alpha = \arcsin(\mathrm{NA})$ is the half-angle of the focusing cone produced by an objective of numerical aperture NA, λ denotes the illumination wavelength, and z and r are the coordinates in propagation and radial direction, respectively. In our simulation, the illuminating light is assumed to have a Gaussian-beam profile with the beam waist matched to the objective's aperture.

Let us define a function $P(r, z)$ that describes the probability of a photon scattered at a depth z and radial location r to pass through the pinhole and to contribute to the detected signal. The function $P(r, z)$ describes depth discrimination, resolution, and stray-light rejection properties of confocal imaging. It is nonzero only within a confined volume, defined by a radius $R(z)$. Light scattered outside this active volume does not contribute to the detected signal unless an additional scattering event takes place. $P(r, z)$ peaks in the focal plane, $z = d$, and decreases with increasing distance from the focus.

The active volume consists of two conical regions symmetrical to the focal plane. From geometrical optics, the boundaries of this active volume are described by

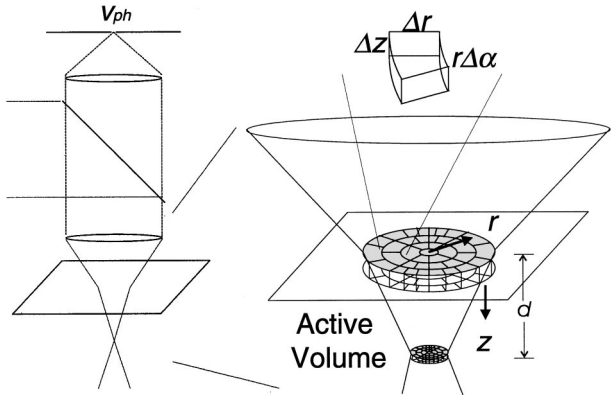

Fig. 1. Schematic diagram of confocal imaging through scattering layers. The volume region from which light can be scattered into the pinhole is subdivided into voxels.

$$R(z) = r_0 + |d - z|\tan\left(\arcsin\frac{\mathrm{NA}}{n}\right), \tag{3}$$

where d is the distance between the material surface and the focal plane, r_0 is the radius of the image of the pinhole in the focal plane, and n is the refractive index of the scattering medium.

We subdivide the active volume into volume elements (voxels). All voxels have to be small enough such that $P(r, z)$ is approximately constant within each volume element. Small voxels are required around the focal region, while the voxel size can be gradually increased toward the surface. The axial symmetry suggests voxels that have the shape of partial annuli, cf. Fig. 1, with size parameters Δr, Δz, and $\Delta\phi$. To keep all three voxel dimensions close to equality, we use $\Delta r = R(z)/N_{\mathrm{R}}$, $\Delta z = \Delta r$, and we set $(r\Delta\phi)^{-1}$ equal to $N_R r/R(z)$ rounded to the closest integer. The parameter N_{R} determines the voxel size and therefore the overall number of voxels. For example, for $N_{\mathrm{R}} = 3$, each disk of voxels consists of one center voxel, 6 voxels in the inner annulus, and 13 voxels in the outer annulus for a total of 20 voxels per disk. For the simulation results reported here, $N_{\mathrm{R}} = 6$ is used. The total number of voxels in the active volume depends on focus depth d as well as on the numerical aperture NA. For a scattering volume extending to infinity along the optical axis, the active volume is also infinitely large. However, for scattering densities $\mu d \geqslant 1$, as examined in the context of this paper, it is sufficient to extend the active volume to twice the distance from the surface to the focal plane. One can estimate the total amount of light singly scattered in this volume and compare it with light singly scattered from greater depths (to infinity). For scattering densities $\mu > 1$, this ratio becomes <0.02.

For $N_{\mathrm{R}} = 6$, $d = 500\,\mu$m, and NA $= 0.4$, for example, the active volume is subdivided into $M = 18\,430$ voxels.

The simulation divides the photons into three groups—(i) singly scattered photons, (ii) doubly scattered photons, and (iii) multiply scattered photons, whose probabilities to reach the detector are calculated separately and summed. The contribution of singly scattered light to the detected signal can be precisely determined. The intensity of unscattered light is known to decrease exponentially with z, and for each voxel the amount of light being scattered into the pinhole $P(r, z)$ is calculated. The depth-resolved response based on single scattering is obtained by summing all voxels at a particular depth z. To define contrast, the amount of singly scattered light reaching the pinhole from inside the confocal region ($\Delta u = \pm 2.8$ optical units[13]) is regarded as the useful signal Σ_{signal}. Light scattered once but outside of the focal region contributes to the noise Σ_{noise}.

The directly illuminated volume is identical to the active volume from which light can be scattered into the pinhole. Hence for doubly scattered light to reach the detector, both scattering events must lie within the active volume. All combinations of voxels need to be considered, with one voxel scattering a fraction of the illuminating light to a second voxel that in turn scatters part of that light into the pinhole. Double scattering can also occur within one voxel, yielding M^2 possible photon paths.

Light scattered more than once is assumed to contribute to the detection noise Σ_{noise} regardless of the location of the scattering sites.

In order to describe the influence of stray light that is scattered three and more times, a refined MC simulation technique[9] is applied in conjunction with the above-described discretized active-volume approach. Before simulating N_{MC} random photon paths through the scatterer, each photon is assigned an initial weight $w_{\text{MC}} = 1/N_{\text{MC}}$. With $\alpha = \arcsin(\text{NA}/n)$, the location of the first scattering event $z^{(1)}$, $r^{(1)}$ is obtained by

$$z^{(1)} = -\frac{\ln(1 - q_z)}{\mu}\cos\left\{\arctan\left[q_r\left(\tan\alpha - \frac{r_0}{d}\right)\right]\right\}, \quad (4)$$

$$r^{(1)} = q_r\left[r_0 + |d - z^{(1)}|\left(\tan\alpha - \frac{r_0}{d}\right)\right], \quad (5)$$

where $0 \leqslant q_z, q_r \leqslant 1$ are random numbers, r_0 is the radius of the image of the pinhole in the focal plane, and μ is the scattering density.

Because of the cylindrical symmetry, only radial and axial coordinates need to be considered for the first scattering location.

At a depth $z^{(1)}$, the probability of a photon being scattered toward the medium's surface and exiting without being scattered again is given by[9]

$$p_{\text{esc}}(z^{(1)}) = \frac{1}{2}[\exp(-\mu z^{(1)}) - \mu z^{(1)} E_1(\mu z^{(1)})], \quad (6)$$

where E_1 is the exponential integral function[14]

$$E_1(x) \approx \begin{cases} -(\ln x + \gamma) + x - \dfrac{x^2}{4} + \dfrac{x^3}{18} & x < 1.618 \\ \dfrac{\exp(-x)}{x}\left(1 - \dfrac{1}{x} + \dfrac{2}{x^2}\right) & x > 1.618 \end{cases}$$

and $\gamma \approx 0.5772$ is the Euler constant. The photon weight w_{MC} is multiplied with $[1 - P_{\text{esc}}(z^{(1)})]$, which yields the weight of the photon that remains in the material and undergoes further scattering.

The location of the second scattering event is determined by simulating the direction (θ, ϕ) and propagation length l relative to the first scattering event. The azimuthal angle θ is simulated by $\cos\theta = 1 - 2q$, while the horizontal angle $\phi = 2\pi q$ is uniformly distributed. Because the escape probability has already been subtracted, Eq. (6), the photon must not leave the scattering medium. The distance l to the next scattering event is therefore dependent on the scattering direction:

$$l = -\frac{\ln(1 - Kq)}{\mu}, \quad (7)$$

with

$$K = \begin{cases} 1 - \exp(-\mu z/\sin\theta) & 0 < \theta \leqslant \pi/2 \\ 1 & 0 \geqslant \theta \geqslant -\pi/2 \end{cases}.$$

The factor K varies with scattering direction θ relative to the surface normal $\hat{z}$ such that the photon's traveling length l is always shorter than the distance to the surface in travel direction l.

From the new scattering location, the probability to reach the pinhole by means of another scattering event in any active-volume voxel is calculated, and all photon-path probabilities are added. The photon weight w_{MC} is multiplied with the so-obtained total path probability to obtain the photon's stray-light contribution.

Before the next scattering event is simulated, the escape probability $p_{\text{esc}}(z^{(2)})$ [cf. Eq. (6)] is calculated for the second scattering location and the photon weight w_{MC} is multiplied with $[1 - p_{\text{esc}}(z^{(2)})]$. The photon undergoes multiple scattering events until the remaining photon weight w_{MC} falls below a preset threshold, or a maximum number of scattering events is reached. The simulation stops after N_{MC} random photon paths have been traced.

In previous MC-based simulations, photons had to reach the pinhole by chance. Thus the number of necessary photon trajectories had to increase with decreasing pinhole diameter to obtain statistically reliable predictions.[10–12] In contrast, in our simulation all considered photon paths end in the pinhole and are weighted according to their individual probability. By summing over path probabilities from each scattering site to the pinhole, reliable predictions are made regardless of optical parameter values. The prediction accuracy of our simulation technique is thus independent of pinhole size and scattering density. Tabulating $P(r, z)$ for all voxels increases the speed of the algorithm. The scheme can easily be extended to include anisotropic scattering ($g \neq 0$) by including tables with direction-dependent scattering probabilities.

Our simulation also allows one to describe the propagation and scattering of light pulses. By referring the photon paths to a common reference, path lengths can be converted to arrival-time differences at the pinhole.

To validate our simulation with experimental data, we measure the confocal signal through a scatterer in reflection mode. The sample consists of a 3-mm-thick suspension of polystyrene spheres ($D = 143$ nm and $g = 0.15$ at $\lambda = 630$ nm) in front of a mirror onto which the light is focused. To compare the measurements with our simulation results, the scattering coefficient μ is corrected by $\mu(1 - g)$. The confocal response is measured for an objective with NA = 0.14.[15] Figure 2 depicts the measured confocal response and the predicted confocal signal from our simulation. The simulated response, when we take

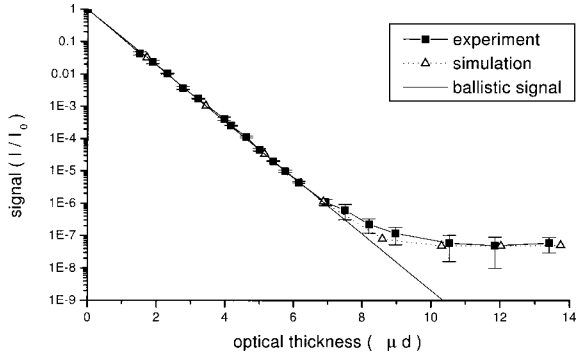

Fig. 2. Experimental measurements and simulation results of the confocal signal when imaging through a scatterer. A mirror in the focal plane reflects ballistic and scattered photons.

into account the mirror in the focus, compares well with our measurements given the fact that the scattering is not completely isotropic.

3. RESULTS

Our simulations concentrate on the discussion of the ability of reflection-mode confocal microscopy to resolve differences in scattering density. While the scattering density is set constant throughout the scattering medium, we regard as useful signal the amount of light being scattered once within the confocal region, Σ_{signal}. Light passing through the pinhole that is scattered more than once or that is scattered outside the confocal region contributes to the noise signal Σ_{noise}. The contrast is defined as

$$C = \frac{\Sigma_{\text{signal}}}{\Sigma_{\text{noise}}}. \tag{8}$$

While the presented simulation method can be extended to $g \neq 0$, previous work indicates that isotropic scattering represents a lower limit with regard to contrast as defined above.[12] For a rough estimation of the effect of anisotropy on C, we replace the scattering coefficient μ by $\mu(1-g)$, where $g \in (0,1)$ is the anisotropy parameter. Let us further consider only singly scattered light and simplify the confocal response by accepting only light from depths $(0 \leqslant z \leqslant 2d)$. In this case

$$C(g) \propto \frac{2\mu(1-g)}{\sinh[2\mu(1-g)]}.$$

For the parameter range of interest C increases with increasing g. As shown previously, however, another imaging characteristic, the resolution, deteriorates with increasing anisotropy.[16]

In all simulations, a pinhole diameter of $v_{\text{ph}} = 2$ optical units is used to ensure confocal imaging characteristics. The focal length of the objective is $f = 5$ mm, and the lens is assumed to be corrected for a water layer of $d = 500\,\mu$m (refractive index $n = 1.33$). The optical thickness μd denotes the average number of scattering events from the surface to the focal plane.

The confocal imaging contrast is examined first for the case of continuous-wave illumination without time gating. The detected light intensity Σ_{total} is composed of the singly scattered signal from the confocal region, Σ_{signal}, and the noise signal $\Sigma_{\text{noise}} = \Sigma_{\text{total}} - \Sigma_{\text{signal}}$. The image contrast C is depicted for different numerical apertures in Fig. 3. Note that at low scattering densities, the contrast increases only moderately with the numerical aperture NA. For constant focus depth d, the relative amount of light scattered outside the confocal region increases with increasing NA, counteracting the increased rejection capability of larger NA. On the other hand, the range of scattering densities where imaging is possible $(C > 1)$ increases with greater numerical apertures. For NA $= 0.2$, confocal contrast is lost at $\mu d = 2$, while imaging through $\mu d = 3.8$ is possible for NA $= 0.8$. The broad confocal region for low numerical apertures allows a substantial fraction of multiply scattered light to pass through the pinhole, diminishing contrast at relatively low scattering densities. At high numerical apertures, on the other hand, the amount of light scattered near the surface overwhelms the singly scattered light from the focal region at high scattering densities. This is illustrated in Fig. 4, where the signal is depicted as a function of the depth of the last scattering event before it passes through the pinhole. The smoothness of the curves in Fig. 4 also illustrates the prediction accuracy obtained by our simulation method. Even though the signal from the sample surface dominates at large scattering densities, a distinct peak from the focal region can be observed.

To discriminate the photons that were scattered near the focus, time-gating techniques have been applied in conjunction with confocal microscopy.[17,18] Our model allows the temporal dependence of the detected signal to be examined because the photon path lengths and radial input and output locations of the photon trajectories are known. Assuming a chromatically corrected objective, we chose a sphere of radius d around the focus and inside the scatterer as a path-length reference from which travel-time differences to the detector are deduced. The small achromatic component due to the radius-dependent residual thickness between this sphere and the sample surface can safely be neglected. In this way a relative travel time and dispersive path is assigned to each photon that passes through the pinhole.

Time-gating techniques cannot directly differentiate between photons from different depths, but rather, they sort photons whose arrival times fall within a certain win-

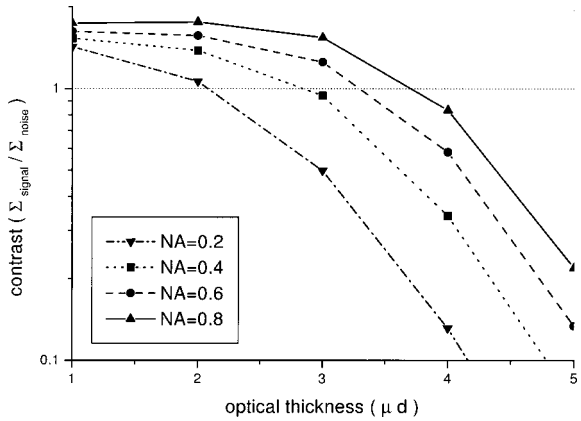

Fig. 3. Confocal imaging contrast C as a function of the optical thickness μd for different numerical apertures NA.

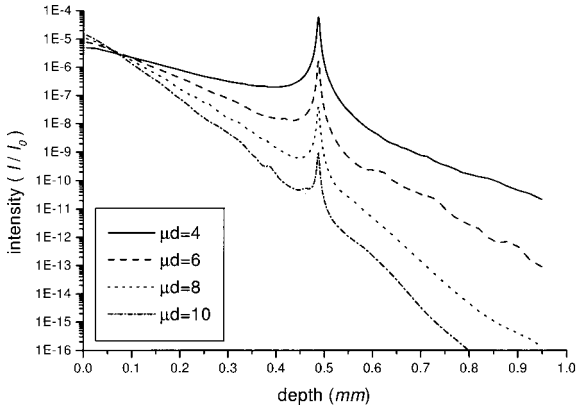

Fig. 4. Normalized confocal signal versus depth for different scattering densities (NA = 0.4).

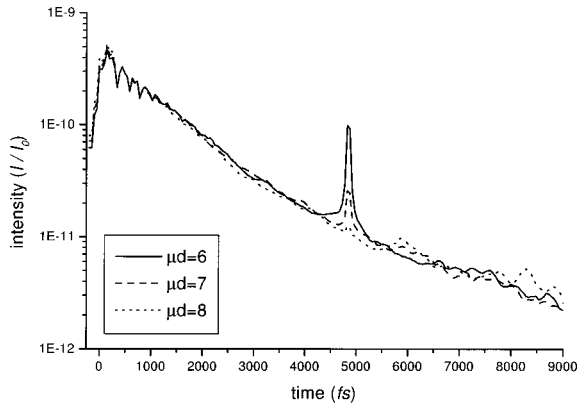

Fig. 5. Confocal imaging with time gating (NA = 0.4). The normalized signal is shown as a function of the position of the time gate for different scattering densities. The oscillations around $t = 0$ originate from the large voxel sizes on the sample surface.

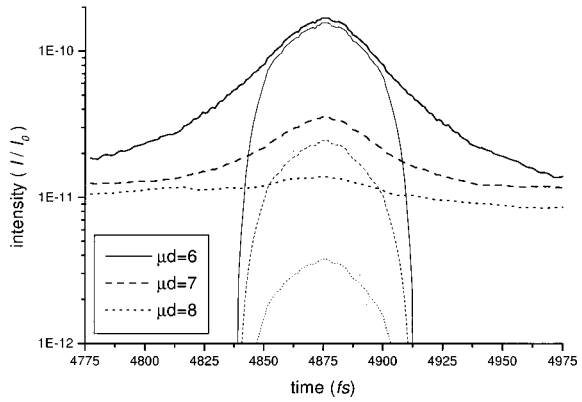

Fig. 6. Same as Fig. 4, depicting the time around focus in detail. The singly scattered signal contribution is shown in addition to the total signal.

dow depending on the width and temporal position of the gate. Figure 5 shows the time-resolved response of reflection-mode confocal microscopy for different optical thicknesses and NA = 0.4. The detected signal is plotted as a function of the time at which the gate is centered. The peak corresponding to the signal from the focal region disappears between $\mu d = 7$ and $\mu d = 8$, which indicates that even with time-gating techniques, confocal imaging is possible only up to about $\mu d = 8$. These values are lower than those measured earlier and estimated from a single-scatter theory.[19] The reason for the discrepancy is that a reflecting object was used, which enhanced the contrast by several orders of magnitude. Figure 6 shows the response for time-gate positions close to the moment when the signal from the focus is expected. At about $\mu d = 7$, the background and the focus signal (singly scattered) are of similar magnitude, while for higher optical thicknesses, the confocal signal drops below the multiply scattered light that has traveled the same total path length, $2d$, but has never reached the focal region. Note that Fig. 4 can easily be misinterpreted: Even though a peak of light scattered from the focal region is obvious, it cannot be discriminated by time-gating means for $\mu d > 8$ (cf. Fig. 5).

Time gating still permits confocal imaging through considerably denser scatterers than without time gating. The optimum time gate is centered at about the expected time of arrival of light from the focal plane. Figure 7 depicts image contrast for different time-gate widths for NA = 0.4 and a duration of the illuminating pulse of 10 fs. Here, contrast is defined as the ratio of singly scattered light from the focal region arriving within the time gate to the signal from multiple scattering that arrives during the gate interval. The contrast improves significantly with decreasing time-gate width. Also, the maximum scattering density increases with shorter gates. If the time-gate width is chosen close to the original pulse length, the maximum scatterer thickness is $\mu d = 7.5$.

Material dispersion was taken into account in the simulations, yet for 10-fs pulses and 1-mm overall path length in water, pulse broadening is negligible. We estimated the dispersive effect of scattering in the case of the strongly wavelength-dependent Rayleigh scattering, where the scattering coefficient is proportional to ω^4. For scattering densities $2\mu d \leqslant 16$ the ballistic component of a 10-fs pulse is broadened by less than 20%. Dispersion of short light pulses by absorption, which could have a stronger effect, was not considered in our simulation, since scattering was assumed to be the primary loss mechanism.

The influence of the numerical aperture on time-gated confocal microscopy is shown in Fig. 8. The contrast in-

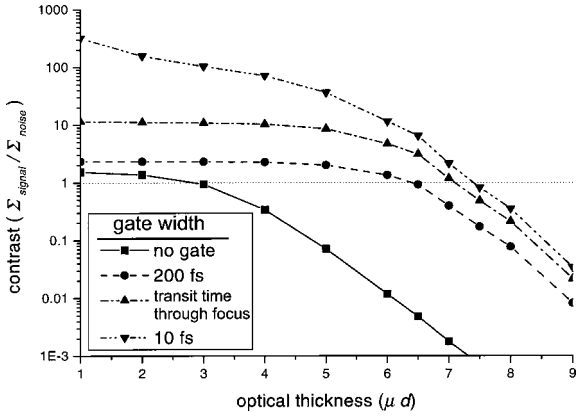

Fig. 7. Comparison of the confocal imaging contrast without (cw) and with time-gating for NA = 0.4. The contrast is determined for 10-fs and 200-fs time-gate widths and for a time-gate width equal to the transit time of light through the focal region ($\Delta u = 5.6$).

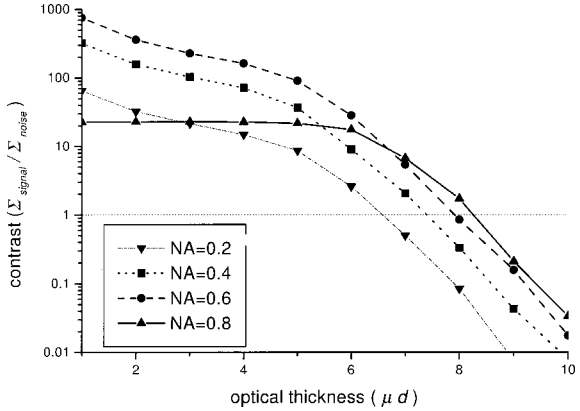

Fig. 8. Confocal imaging contrast using a 10-fs time gate for different numerical apertures.

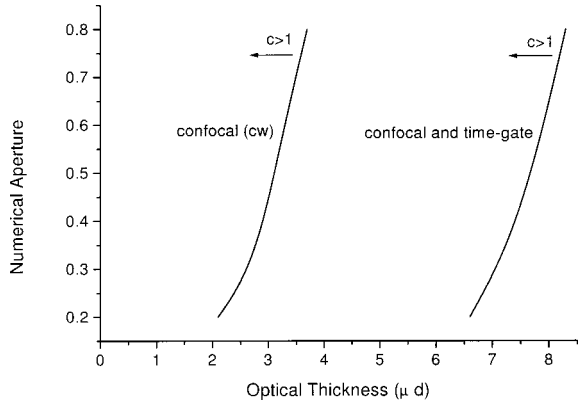

Fig. 9. Confocal imaging without and with a 10-fs time gate. The curves describe the parameter combination at which the contrast $C = 1$. Confocal imaging is possible to the left of the respective curves.

creases with numerical aperture up to a value of NA $\approx$ 0.6. When the transit time through the focal region ($\Delta u = 5.6$) becomes shorter than the time-gate width, the gating becomes less efficient as more (undesired) light from outside the confocal region is recorded. This results in a decrease in contrast that becomes obvious for NA = 0.8. The maximum scattering thickness, however, increases monotonously with numerical aperture independent of the gate width.

Figure 9 summarizes our results and compares the performance of confocal microscopy with and without time gating. Imaging is possible for $C > 1$, which corresponds to the parameter ranges to the left of the respective curves.

4. CONCLUSIONS

A novel simulation method has been developed for the study of confocal imaging characteristics with and without time gating. Our simulations show that confocal microscopy alone can image through isotropic scattering media of up to $\mu d \approx 3.5$ optical thickness if high numerical aperture objectives are used. Time gating the detector yields better contrast due to a more efficient rejection of scattered light. Imaging through greater scattering densities thus becomes possible. The time-gate width should be smaller than the transit time of the pulse through the confocal region for optimum performance. Time-gating methods are limited by the amount of stray light reaching the detector during the same time interval as the focus signal. Our simulations show that this point is reached at an optical thickness of about $\mu d = 8$ for NA = 0.8. The maximum scattering densities obtained in our simulation are in good agreement with the measurements described in Ref. 17. Our simulation also reproduces the fact that the single-scatter model overestimates the scatter rejection.

Due to the assumption of isotropic scattering ($g = 0$) and our contrast definition that assumes that only singly scattered light from the confocal region represents useful signal (i.e., no scatter enhancement from the object is assumed), our results describe the lower limits of confocal imaging through scattering media with and without time gates.

ACKNOWLEDGMENT

This project was supported in part by the National Foundation for Functional Brain Imaging (NFFBI).

The e-mail address for Marcus Magnor is magnor@stanford.edu. The e-mail address for Wolfgang Rudolph is wrudolph@unm.edu.

REFERENCES

1. J. G. Fujimoto, S. de Silvestri, and E. P. Ippen, "Femtosecond optical ranging in biological tissue," Opt. Lett. **11**, 150–152 (1986).
2. J. M. Schmitt, "Optical coherence tomography (OCT): a review," IEEE J. Sel. Top. Quantum Electron. **5**, 1205–1215 (1999).
3. K. M. Yoo, Feng Liu, and R. R. Alfano, "Biological materials probed by the temporal and angular profiles of the backscattered ultrafast laser pulses," J. Opt. Soc. Am. B **7**, 1685–1693 (1990).
4. R. Vreeker, M. P. Van Albada, R. Sprik, and A. Lagendijk, "Femtosecond time-resolved measurements of weak localization of light," Phys. Lett. A **132**, 51–54 (1988).
5. E. Baiger, C. Hauger, and W. Zinth, "Imaging within highly scattering media using time-resolved backscattering of femtosecond pulses," Appl. Phys. B **67**, 257–261 (1998).
6. M. Kempe, A. Z. Genack, W. Rudolph, and P. Dorn, "Ballistic and diffuse light detection in confocal and heterodyne imaging systems," J. Opt. Soc. Am. A **14**, 216–223 (1997).
7. M. S. Patterson, B. Chance, and B. C. Wilson, "Time resolved reflectance and transmittance for the non-invasive measurement of tissue optical properties," Appl. Opt. **28**, 2331–2336 (1989).
8. S. T. Flock, M. S. Patterson, B. C. Wilson, and D. R. Wyman, "Monte Carlo modeling of light propagation in highly scattering tissue I: Model predictions and comparison with diffusion theory," IEEE Trans. Biomed. Eng. **36**, 1162–1167 (1989).
9. E. Tinet, S. Avrillier, and J. M. Tualle, "Fast semianalytical Monte Carlo simulation for time-resolved light propagation in turbid media," J. Opt. Soc. Am. A **13**, 1903–1915 (1996).
10. J. M. Schmitt, A. Knüttel, and M. Yadlowsky, "Confocal microscopy in turbid media," J. Opt. Soc. Am. A **11**, 2226–2235 (1994).
11. J. M. Schmitt and K. Ben-Letaief, "Efficient Monte Carlo simulation of confocal microscopy in biological tissue," J. Opt. Soc. Am. A **13**, 952–961 (1996).
12. C. M. Blanca and C. Saloma, "Efficient analysis of temporal broadening of a pulsed focused Gaussian beam in scattering media," Appl. Opt. **38**, 5433–5437 (1999).
13. T. Wilson, ed., *Confocal Microscopy* (Academic, San Diego Calif., 1990), p. 11.
14. H. C. Van De Hulst, *Multiple Light Scattering: Tables, Formulas, and Applications* (Academic, San Diego, Calif., 1980), Vol. 1, p. 9.
15. M. Magnor, "Reflection mode confocal microscopy through scattering media," M.S. thesis (University of New Mexico, Albuquerque, New Mexico, 1997), p. 63.
16. J. M. Schmitt and A. Knüttel, "Model of optical coherence tomography of heterogenous tissue," J. Opt. Soc. Am. A **14**, 1231–1242 (1997).
17. M. R. Hee, J. A. Izatt, J. M. Jacobson, and J. G. Fujimoto, "Femtosecond transillumination optical coherence tomography," Opt. Lett. **18**, 950–952 (1993).
18. A. Schmidt, R. Corey, and P. Saulnier, "Imaging through random media by use of low-coherence optical heterodyning," Opt. Lett. **20**, 404–406 (1995).
19. M. Kempe, W. Rudolph, and E. Welsch, "Comparative study of confocal and heterodyne microscopy for imaging through scattering media," J. Opt. Soc. Am. A **13**, 46–52 (1996).